Stefano Sfarra*, Clemente Ibarra-Castanedo, Carlo Santulli, Domenica Paoletti and Xavier Maldague

Monitoring of jute/hemp fiber hybrid laminates by nondestructive testing techniques

Abstract: Damage following static indentation of jute/hemp (50 wt.% total fiber content) hybrid laminates was detected by a number of nondestructive testing (NDT) techniques, in particular, near (NIR) and short-wave (SWIR) infrared reflectography and transmittography, infrared thermography (IRT), digital speckle photography (DSP), and holographic interferometry (HI), to discover and evaluate real defects in a laminate with a complex structure. A comparative study between thermographic data acquired in the mid- (MWIR) and long-wave infrared (LWIR) spectrum bands, by pulsed (PT) and square pulse (SPT) thermography, is reported and analyzed. A thermal simulation by COMSOL® Multiphysics (COMSOL Inc., Burlington, MA, USA) to validate the heating provided is also added. The robust SOBI (SOBI-RO) algorithm, available into the ICALAB Toolbox (BSI RIKEN ABSP Lab, Hirosawa, Japan) and operating in the MATLAB® (The MathWorks, Inc., Natick, MA, USA) environment, was applied on SPT data with results comparable to the ones acquired by several thermographic techniques. Finally, segmentation operators were applied both to the NIR/SWIR transmittography images and to a characteristic principal component thermography (PCT) image (EOF_s) to visualize damage in the area surrounding indentation.

Keywords: bast fibers; damage characterization; infrared vision; optical NDT techniques; static indentation.

DOI 10.1515/secm-2013-0138
Received June 12, 2013; accepted September 6, 2014; previously published online November 28, 2014

***Corresponding author: Stefano Sfarra,** Las.E.R. Laboratory, Department of Industrial and Information Engineering and Economics (DIIIE), University of L'Aquila, Piazzale E. Pontieri no. 1, 67100 Monteluco di Roio, L'Aquila (AQ), Italy,
e-mail: stefano.sfarra@univaq.it
Clemente Ibarra-Castanedo and Xavier Maldague: Computer Vision and Systems Laboratory (CVSL), Department of Electrical and Computer Engineering, Laval University, 1065, av. de la Médecine, G1V 0A6 Québec city (QC), Canada
Carlo Santulli: School of Architecture and Design (SAD), University of Camerino, Viale della Rimembranza, 63100 Ascoli Piceno, Italy
Domenica Paoletti: Las.E.R. Laboratory, Department of Industrial and Information Engineering and Economics (DIIIE), University of L'Aquila, Piazzale E. Pontieri no. 1, 67100 Monteluco di Roio, L'Aquila (AQ), Italy

1 Introduction

In recent years, plant fibers are increasingly employed as reinforcement for panels and semistructural components, with the idea to improve materials biodegradability and end-of-life scenarios [1]. In trying to broaden the field of application of these materials, more stringent mechanical and impact/indentation resistance criteria are required [2]. In spite of the growing interest in these materials, fiber selection is still prevalently based on economical factors and local availability rather than on materials properties.

Indentation resistance in composites refers to the ability to withstand damage induced by loading contact of a foreign body on a material. This includes the study of the failure modes, initiation, development, and extent of damage subsequent to contact with an indenting body, which normally initiates in laminated composites in the form of transverse matrix cracking, followed by delamination, fiber/matrix debonding, and fiber fracture [3]. This kind of damage substantially reduces the residual strength of a composite structure, even when it cannot be visually observed, such as is often the case in plant fiber composites. For this reason, nondestructive testing methods, such as optical and infrared techniques, have been applied to the defect detection after an indentation test of jute/hemp fiber hybrid laminates. In biological materials, the combined presence of stronger and weaker components is a natural procedure developed during evolution to obtain the maximum possible impact resistance [4]. This means that plant fibers can work effectively through the limited and controlled occurrence of defects, which are irregularly spaced along their length. As a result, the tensile strength of the fibers decreases with their length, and a pronounced strain rate effect would also be observed: this has an effect, albeit not easily predictable, also on the indentation resistance of plant fiber composites [5]. Most studies, so far, have been concerned with either improving fiber quality or reducing the effect of the presence of fiber defects on the final material via improved processing or fiber treatment [6–8]. It can be suggested that defects have a more central role in

affecting impact properties in plant fiber composites than in glass fiber composites [8].

An integrated approach between IRT, DSP, and HI, recently applied to glass and basalt fiber composite materials to study their behavior following low velocity impacts [9], was experimented in the present work. On these hybrid composites, this method combined with other IR equipment, and/or advanced signal processing allows predicting initiation and development of the phenomena leading to its failure and offers a comparative evaluation of the different damage modes of hybrid laminates. An advanced signal processing is also used [robust SOBI (SOBI-RO) algorithm], which combines robust whitening and time-delayed decorrelation. It was applied using the same number of frames as for the PCT algorithm for reference: the comparison between the results obtained is described in the Materials and methods section. This algorithm, introduced in [10], improves the classical SOBI method [11] by integrating robust whitening [10, 12, 13], instead of simple whitening, the main objective being the elimination of the influence of the white noise. The use of the *distance transform* enables to visualize on a final image the areas of the sample with a lower concentration of fibers. The latter considerations are also operative if a characteristic PCT image (EOF_s) is first segmented using the marker-controlled watershed operator and, second, smoothed by *top-hat* transform. A preventive thermal simulation is needed to highlight the thermographic results. After this, a comparison among several techniques applied on pulsed thermography (PT) data, namely, higher-order statistic thermography (HOST), pulsed phase thermography (PPT), principal component thermography (PCT), and IR correlation, is required. This comparison will serve both as validation of the integrated method proposed and for the detection of zones with lack of fibers/resin starved, zones with a higher concentration of fibers, and to detect the boundary line linked to these with the aid of *distance transform*.

2 Nondestructive testing (NDT) methods

In Table 1, the fundamental technical information, as well as the advantages and disadvantages of the various NDT methods used in this work are reported.

Spatial resolution refers to the size of the smallest object that can be resolved on the ground. In our case, the smallest interesting object is likely to be a detected defect. Different factors influence the retrieve of a defective area: for example, using the HI technique, the sensitivity is reduced as defect depth increases, while in a digital image, the smallest resolvable object cannot be smaller than the pixel size, which is determined by the sampling distance.

References for sounder knowledge of each NDT method used are reported below: ***digital speckle photography (DSP)*** [15–29], *particle image velocimetry (PIV)* software (MatPIV 1.6.1, Free Software Foundation, Inc., Boston, MA, USA) and/or 2D-PIV software ver. 3.001-1.11) [30–32], ***holographic interferometry (HI)*** [33–42], *double-exposure HI* [43, 44], ***near/short-wave infrared inspection (NIR/SWIR)*** [45, 46], *distance transform (DT)* [47, 48], ***pulsed thermography (PT)*** [49], *correlation coefficient (IR correlation)* [50–53], *pulsed phase thermography (PPT)* [54, 55], *higher-order statistics thermography (HOST)* [56–58], ***square pulse thermography (SPT)*** [59–62], *principal component thermography (PCT)* [63–68], *top-hat transform* [69], *watershed transform* [70, 71], and *robust second-order blind identification (SOBI-RO)* [72, 73]. The techniques written in *italics* have been applied to the methods written in ***bold italics***. The experimental setups of the methods applied are reported in Figures 1A–F along with a schematization of the PPT techniques (Figure 1E).

3 Materials and methods

The laminate tested in this work has been manufactured using jute hessian cloth (plain weave) of areal weight 250 g/m^2, obtained locally, and hemp fibers, supplied by AMCO (Cairo, Egypt), decorticated and bleached using sodium chlorite in optimized conditions, impregnated with I-SX10 LEGNO epoxy resin and SX10 LEGNO 33% (Mates Italiana, Segrate (MI), Italy) general purpose hardener, both by Mates Italiana. Epoxy was used as this low-viscosity polymer penetrates easily into the fiber assembly and forms covalent binding to the plant fibers resulting in strong interface. The layup of the indented laminate includes six inner layers of jute plain weave disposed at 0°/0°/45°/-45°/0°/0°, sandwiched between two nonwoven hemp mats. The composite includes 30(±2) wt.% of jute fiber and 20 wt.(±1.5) wt.% of hemp fiber. The laminate was produced using a hand lay-up procedure in a closed matching mold of dimensions 220×250×3.7 (±0.2) mm^3 by applying a slight pressure of ca. 0.02 MPa. The dimensions of the final sample were 140×220×2.8 (±0.1) mm. Static indentation tests were performed using a hemispherical nose of 12.7 mm diameter

Table 1 Fundamental technical information (yellow background), advantage, and disadvantage (green background) of the NDT methods used.

NDT technique	DSP	HI	NIR	SWIR	MWIR	LWIR
			Reflectography		Thermography	Thermography
Processing technique or mode of image acquisition	MatPIV 1.6.1	DE	Image subtractions	Transmittography	IR correlation	Raw thermograms ↕ Thermal simulation
	2D-PIV ver. 3.001-1.11		DT		HOST	SOBI
					PPT	Top-hat DT Watershed T
					PCT	PCT
	Image fusion					
Type of the method	Optical methods		Thermal methods			
Type of the stress applied	Active		Lamp	Lamp	Active	
	Soldering iron				Flash lamps (PT)	Lamp (SPT)
	n° 1				n° 2	n° 1
	50 W	50 W	250 W	Incandescent	Photographic	500 W
	Long heating	Long heating	Short lighting	Short lighting	Short heating	Long heating
Spatial resolution or detector array number of elements	0.2–0.3 mm [14]	>3000 lines/mm	3888×2592 pixels (5.7 µm pitch)	640×512 pixels (25 µm pitch)	0.25 mrad	1.1 mrad
Cost of the equipment	Medium high	Medium high	Medium	Medium	High	Medium high
In situ operation	Good	Very poor	Very good	Very good	Medium	Good
Sensitivity	Medium	High	High	Medium high	Medium high	Medium high
Main advantages	Different types of defects can be detected; shallow defects can be easily detected		Can be transmitted through some insulating and nonconductive materials, and weakly absorbed by others			
			Large surface areas of materials can be inspected rapidly and at low cost in terms of implementation of the measurements; parts with complex geometry are routinely inspected			
Main disadvantages	The detection of deeper defects depends on the material under inspection		Some types of paints can mask subsurface defects		The processing of a large amount of data can be time consuming	

according to ASTM D6264-12 standard on simply supported 110-mm side laminates. Loading has been applied in displacement control with 1 mm/min cross-head speed. Optical and infrared NDT techniques have subsequently monitored the presence of damage due to loading on the whole surface of sample.

The external presence of hemp fibers does not result in the extensive tearing of the laminate along the impact

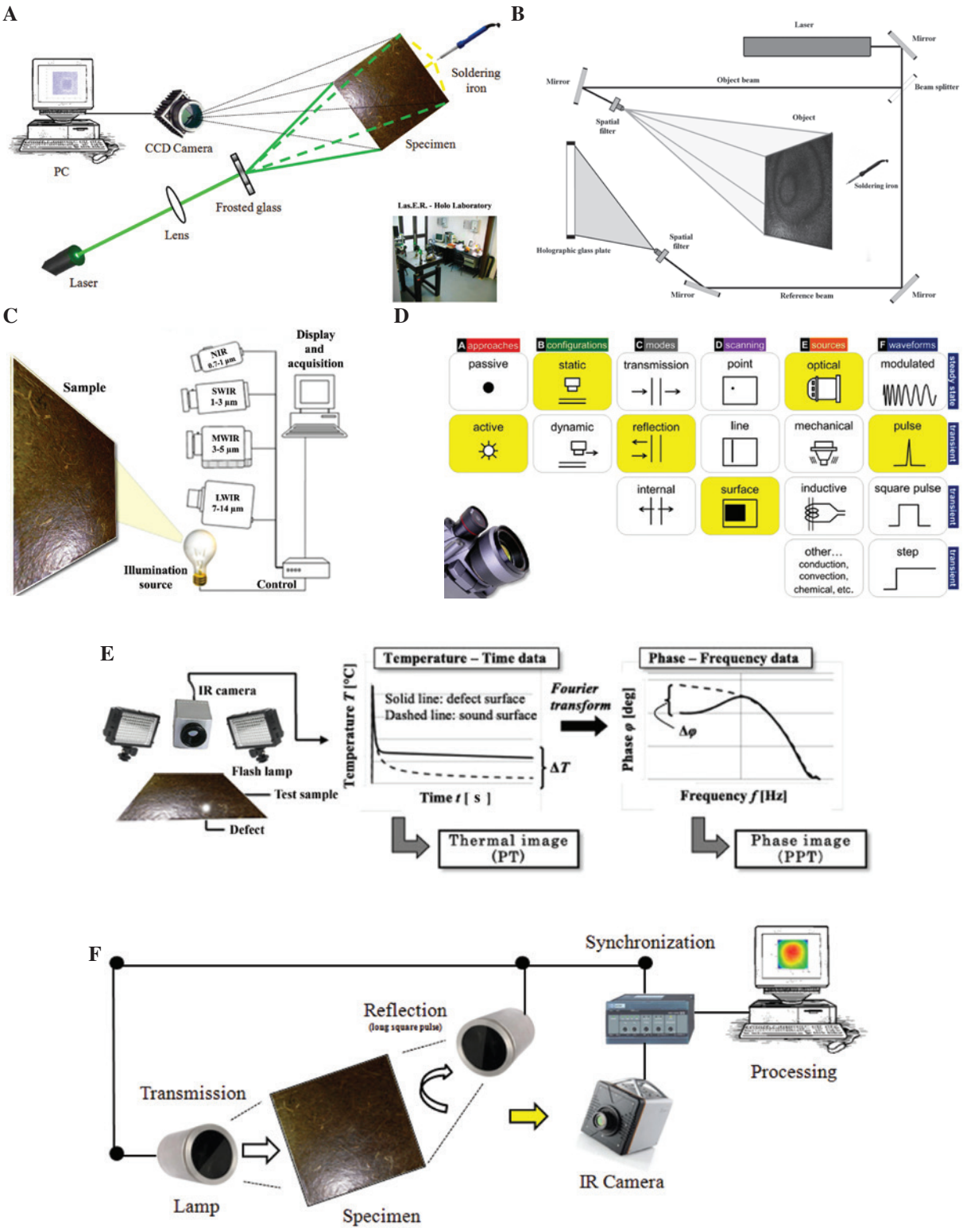

Figure 1 (A) Experimental setup for digital speckle photography (DSP), (B) experimental setup for double-exposure (DE) holographic Interferometry (HI), (C) experimental setup for NIR-SWIR-MWIR-LWIR, (D) classical optical pulsed thermography (PT) [49], (E) inspection and data processing procedure in the pulsed phase thermography (PPT), (F) experimental setup for square pulse thermography (SPT).

loading diameter line, which is a characteristic of impact damage on jute fiber reinforced laminates [74, 75]. This assumption is also confirmed by comparing the NDT experimental results obtained from the indented laminate, which is shown in Figure 2A.

In the present study, one variation of HI was applied, namely, double exposure (DE) technique. In DE-HI, two holograms are recorded on the same fine-grained green sensitive holographic plate (VRP-M) made by Slavich®, (Geola Digital, Vilnius, Lithuania) each one capturing the object in a different state separated by a fixed time interval [43]. Typical values of grain size in the emulsions intended for holographic use are in the order of 0.03–0.08 μm. Emulsions with larger grains yield the highest sensitivity, yet have lower spatial efficiency (resolution), as reported in Table 1, at row 5 column 3. Holographic plates used had dimensions of 10.2×12.7 cm.

In addition, during the interferometric inspection, the interferograms were acquired using a laser product (G4plus250 laser by Elforlight Ltd., Daventry, UK), with a fundamental wavelength of 532 nm, vertical polarization, and a specific power of 250 mW. Double-exposure measurement (distance tip of the soldering iron sample: 25 mm) was performed in transmission mode using a soldering iron station made by *The Cooper group* WELLER® (Apex, NC, USA), WECP-20 type (P_{max}=50 W at 24 V. Accuracy: regulation tolerance±2% of final value). In this version, analog temperature regulation is carried out using a potentiometer, able to set the temperature continuously in the 50–450°C range. A heat conveyor mounted between the soldering tip and the back face of the sample was provided. Because of its extreme sensitivity to surface deformation, HI is well suited to inspect natural fiber composites; as a very small thermal stress is involved here, a surface temperature increase of up to 3°C was used. The interferogram reported in Figure 2B was obtained with the first exposure (t_{exp}=2 s) 10 s after switching off the soldering iron and a second exposure (t_{exp}=2 s) 2 min after the first exposure and a heating time of 3 min. The stressing method is usually selected empirically with guidance provided by an analysis of anticipated deformation or by previous results obtained from simulated models. In the present case, the temperature increase of the sample's surface was monitored by the same thermo-camera used for the SPT data collection. SPT data was acquired working in the LWIR spectrum and using optical excitation.

The cusps of the fringes indicating delaminations due to the indentation test are identified in Figure 2B (red arrows), while minor defects, probably due to strains of compression, are indicated by yellow arrows. Their position reflects the Clark's model shown in Figure 3 [76].

The indentation test produces a local inflection of the lamina, with the consequent production of strains, but while in the indented area, compression forces between the layers predominate, due to the direct action of the hemispherical nose, strains causing delamination are located in the surrounding area. Hence, from the comparison of the experimental results presented in Figure 2B with the model shown in Figure 3, it is apparent that in the A zone (at a 45° angle, which is the direction of the lower-layer fibers), the lower fibers have a strain component directed upward, while in the lower layer, the inflection generates a strain component downward. It may be suggested that a stress state acts in the points of the A

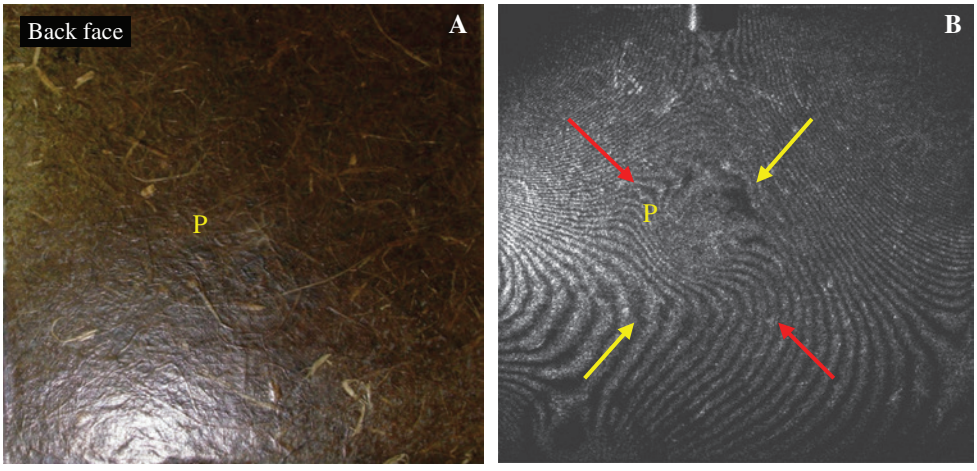

Figure 2 (A) Photo of the sample (back face), (B) DE result of the sample: the red arrows indicate the delaminations due to the indentation test detected by HI, the yellow arrows show the compressed zone, while P the indented area.

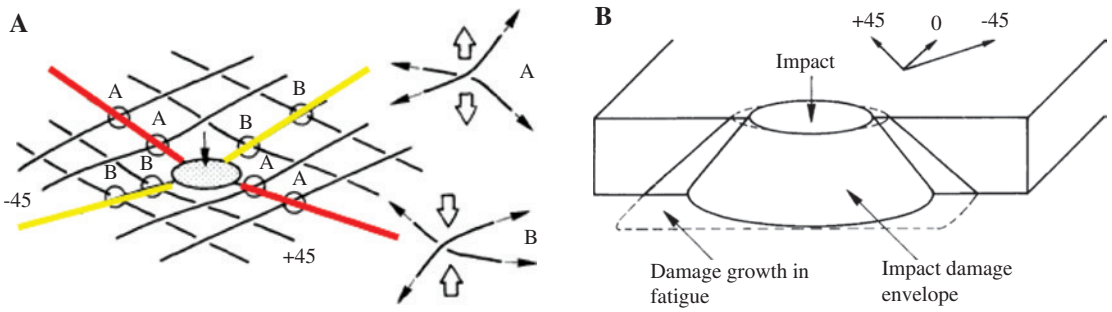

Figure 3 (A) The formation model of delaminations, (B) stress zone due to the indentation test [76].

zone causing the delaminations. Vice versa, compressing strains tend to act into the B zone (in the direction of the fibers of the upper layers, -45°), avoiding in this way the apparition of delaminations.

To study the P indented area (Figure 2A), we used the configuration reported in Figure 1A, which provided the experimental results shown in Figures 4A and B.

In practice, results coming from MATPIV 1.6.1 (Figure 4A) were compared with the results obtained by 2D-PIV ver. 3.001-1.11 (Figure 4B).

The results shown in Figure 4A and B come from the same set of acquisitions (the images were captured every 5 s starting at 10 s after switching off the soldering iron), with the heating time (3 min) also used for the HI experiment. The position of the delaminated and compressed areas, as identified by DE-HI (Figure 2B) and proposed by Clark (Figure 3A) can be confirmed. On the other hand, the contribution of the 2D-PIV software was important to identify the indented area, already visible in Figure 2B (note the change of the fringes pattern near the P area). The indented area analyzed by DSP technique from the rear face of the sample reflects Clark's model reported in Figure 3B. In Figure 5 is reported the SURF result considering part of the sample's surface.

In the present work, the option *multi* has been used, which, using cross-correlation, performs three or more iterations through the images [30].

The size of the sub-images, often selected to be 32×32 or 64×64 pixels, determines both the spatial resolution and the accuracy of the measurement. This consideration is reported in Table 1, row 5 column 2.

The three zones marked by a solid red oval, a solid violet oval, and the P indented area need to be considered, for a subsequent correlation with the SPT results. The figure presents the strain field that was calculated using the *strain* subroutine in MATPIV. In particular, the *circulation* option was employed, which is based on the Sobel's algorithm to recognize gradients. In this case, a SURF plot, similar to a 3D map, was chosen for improved visualization. Repeating the experimental parameters used during the HI experiment, i.e., correlating the image captured 10 s after switching off the soldering iron and the 24th image after the first one, the result proposed in Figure 5 was obtained, which provides integrated information when combined to the HI result (Figure 2B).

During the SPT data acquisition, the sample was heated for 4 min using a 500-W lamp positioned in reflection mode (lamp – sample distance: 35 cm), and the surface cooling

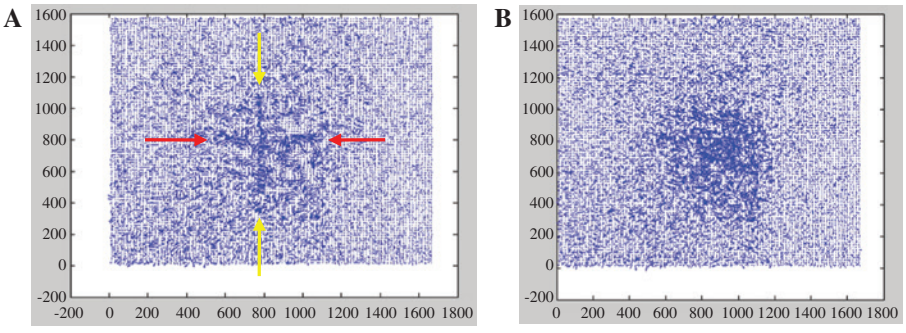

Figure 4 (A) MatPIV 1.6.1 software-QUIVER result (processing of the first and second images after switching off the soldering iron), (B) 2D-PIV software ver. 3.001-1.11-QUIVER result (processing of the first and second images after switching off the soldering iron).

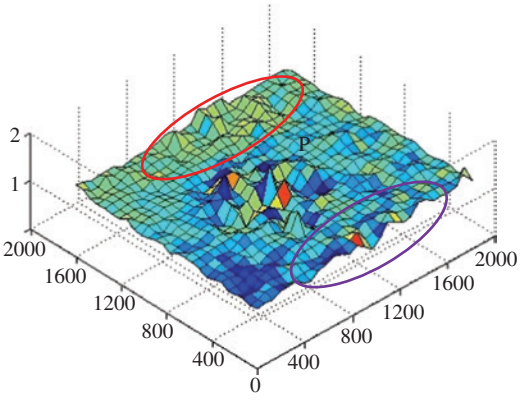

Figure 5 MatPIV 1.6.1 software-SURF result (processing of the first and 24th images after switching off the soldering iron).

down was recorded by an IR camera (FLIR Systems, Wilsonville, OR, USA – ThermaCAM S65 HS). The acquisition was carried on for 780 at the rate of one thermogram per second. In Figure 6, two raw thermograms are reported, which do not appear to provide sufficient information on the considered laminate. Only a slight indication about two subsurface defects can be detected in Figure 6B, while information about the texture of the inner layers cannot be retrieved.

The large energy supply required to follow the thermal performance of the plant fiber composites depend on their complex structure. Bast fibers, which are, in fact, fiber bundles, each contain 10–40 single cells or elementary fibers. A single stem includes 20–50 fiber bundles. The elementary fibers (single cells) of hemp consist of layers, and there is a lumen inside the cell [77, 78]. Natural fiber is filled with porous cellulose material, which acts as an insulator, thus, a natural fiber composite shows lower thermal conductivity k when compared to a glass fiber-reinforced polymer (GFRP) composite [79]. In general, the k (W/m K) value for hemp fibers is between 0.040 and 0.094 (W/m K) [80–82] and between 0.365 and 0.482 (W/m K) for jute fibers [79], since k varies nonlinearly with density [83, 84]. Thermal conductivity of the epoxy resin used is between 0.229 and 0.256 (W/m K) [85].

The laminate was pre-cured at 40°C, then cured at 120°C under a slight pressure. The latter data served to establish the maximum thermal stress to confer to the sample (~73.7°C), aiming at not causing damage to its structure, while allowing sufficient heat conduction through the whole thickness. A summary of the plies thickness and the thermal characteristics of the fibers/resin is reported in Table 2.

Taking into account this data and applying the theoretical model for transverse effective thermal conductivity of Springer and Tsai [87], which assumes that a) matrix and fiber as parallel and series as in electrical circuits, b) fiber patterns as square, cylindrical, and elliptical shapes, the K_{22} (theoretical average value) of the whole sample can be calculated.

The previous considerations inherent in the maximum thermal stress, the information reported in Table 2, the K_{22} parameter, as well as the lack of fibers/resin-starved areas identified along the sides of the sample by using NIR,

Table 2 Schematic summary of the main characteristics of the sample analyzed.

Consecutive number of the plies	Disposition of the fibers	Nature of the fibers	Plies thickness [86]	Thermal conductivity of the fibers (W/m K)
1	Nonwoven mat	Hemp	~0.5	0.040–0.094
2	0°	Jute	~0.3	0.365–0.482
3	0°	Jute	~0.3	0.365–0.482
4	+45°	Jute	~0.3	0.365–0.482
5	−45°	Jute	~0.3	0.365–0.482
6	0°	Jute	~0.3	0.365–0.482
7	0°	Jute	~0.3	0.365–0.482
8	Nonwoven mat	Hemp	~0.5	0.040–0.094

Thermal conductivity of the resin (W/m K): 0.229–0.256 (W/m K).

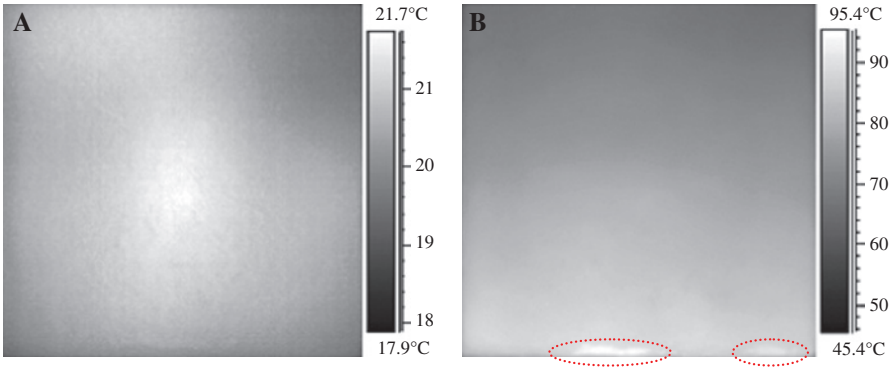

Figure 6 Raw thermograms: (A) at 1 s, (B) at 240 s.

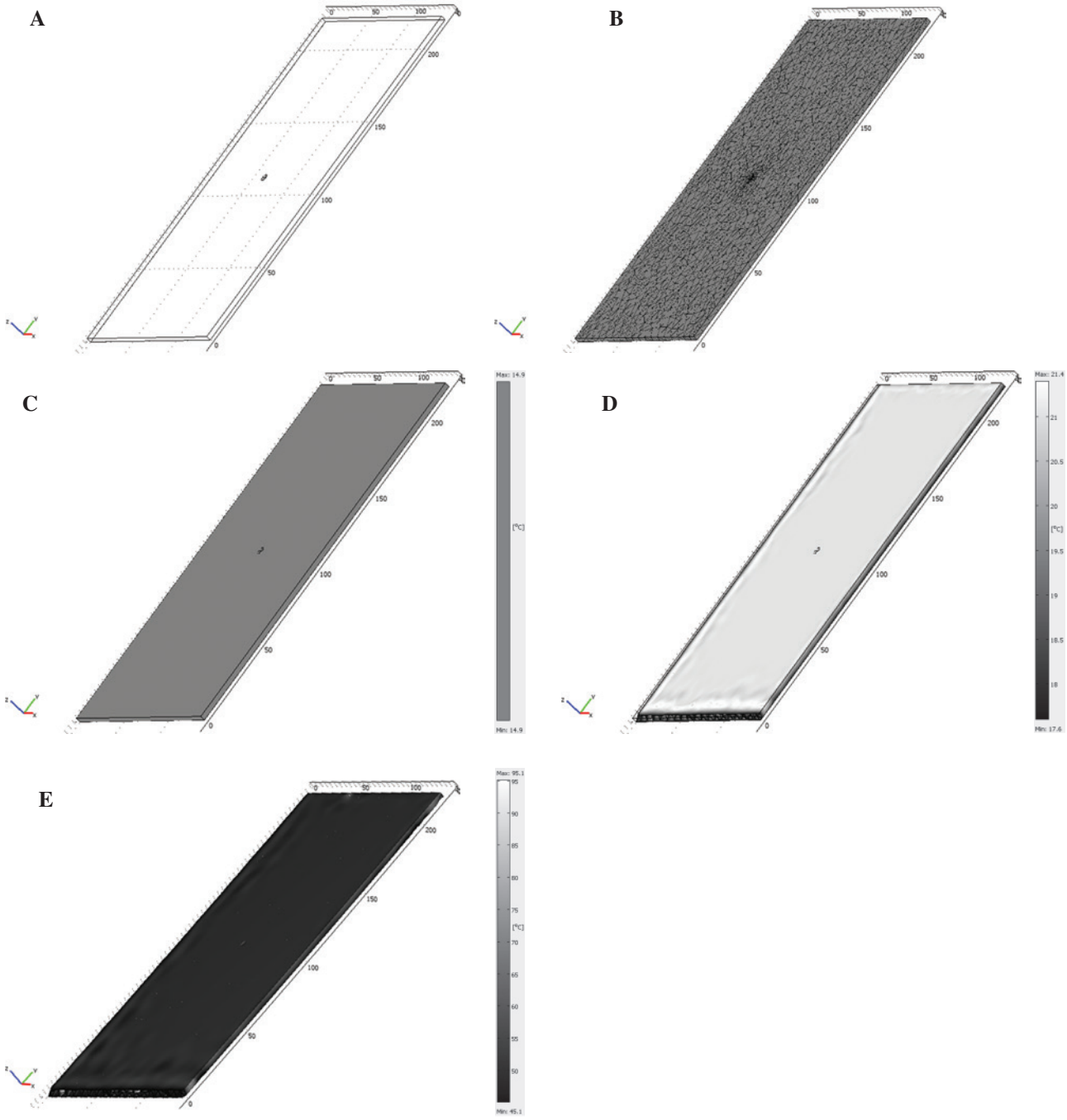

Figure 7 (A) Structure of the indented sample realized by COMSOL®, (B) mesh, (C) temperature (°C) at the steady state, and square pulse (SP): (D) temperature distribution (°C) at 1 s, (E) temperature distribution (°C) at 240 s.

SWIR, and IRT results as explained in the following, have been utilized in order to build a COMSOL® model (Figure 7).

The model allows linking the most important characteristics of the sample with the most important defects retrieved by using thermal (MWIR, LWIR) and nonthermal (NIR, SWIR) infrared vision.

Indeed, the COMSOL® Multiphysics (COMSOL Inc., Burlington, MA, USA) simulation environment facilitates all steps in the modeling process, defining the geometry of the case under analysis (Figure 7A), specifying the physics, meshing (Figure 7B), solving, and then processing/visualizing the input data (Figure 7C–E). The goal of simulation, therefore, was to minimize the difference ("error") between the exact and the approximated solution [88].

Starting from the sample at the steady-state condition (Figure 7C), the simulation shows that after 1 s (Figure 7D)

and 240 s (Figure 7E) of thermal exposures, the maximum and that the minimum temperature values are in good agreement with the temperature scale diagrams of Figure 6. This is the validation of the approximate solution and, in the same time, the confirmation of the good choice of the thermal exposure time correlated to the *z* axis.

It is noteworthy that applying the image contrast function available in the COMSOL® program, the thermal discontinuities along the sides of the sample (marked by arrows in Figures 7D, E) already appear at the early stage of heating.

As previously mentioned, the SPT data was analyzed in the first instance by PCT algorithm, and the main results are reported in Figure 8. In particular, the thermal image sequence containing the information about our sample is processed using singular value decomposition (SVD)-based PCT. The latter reorganizes data into new components accounting for the main spatiotemporal variances of the sequence.

From Figure 8B to D, readers can see the great quality image resolution of the nonwoven mat of hemp, as well as that of the P indented area.

The EOF_s are also correlated with the depth of the defect [67]. The P indented area forms a cut cone inside the sample according to Clark's model (Figure 3B). The greater extension that is possible to see in Figure 8E is linked to the dent damage envelope explained in Figure 3B.

There is correspondence between the second degree in-plane deformation (highlighted in red and purple) caused by the indentation test (P area) in Figure 5, and the dark areas identified by PCT-EOF_6 in Figure 8D. For the defect marked in red (Figure 8D), a change in color (from light to dark) between EOF_4 and EOF_6 is observed, opposite to what happened for the P area, suggesting that the defects are due to different materials [89], including a lack of adhesion between the fibers [86].

In addition, the superposition between the visible image, the DSP-QUIVER result and the PCT-EOF_{14} result (Figure 9), provides a good correspondence between optical and infrared nondestructive testing techniques.

Near-infrared reflectography and transmittography (Figure 10) were applied to confirm the IRT results [90]. The EOF_{10} shows a correlation with the result coming from the NIR processing (Figure 10) and bears some similarity with the DT result (Figure 11D), applied for the first time. To visualize the internal fiber distribution of the sample, the reflectogram has been subtracted to the transmittogram to identify the weak areas using the *distance transform* (DT) operator, as explained below.

A CMOS camera (Canon 40DH 22.2×14.8 mm –10 megapixel 0.38–1.0 μm), with a visible cutoff filter to

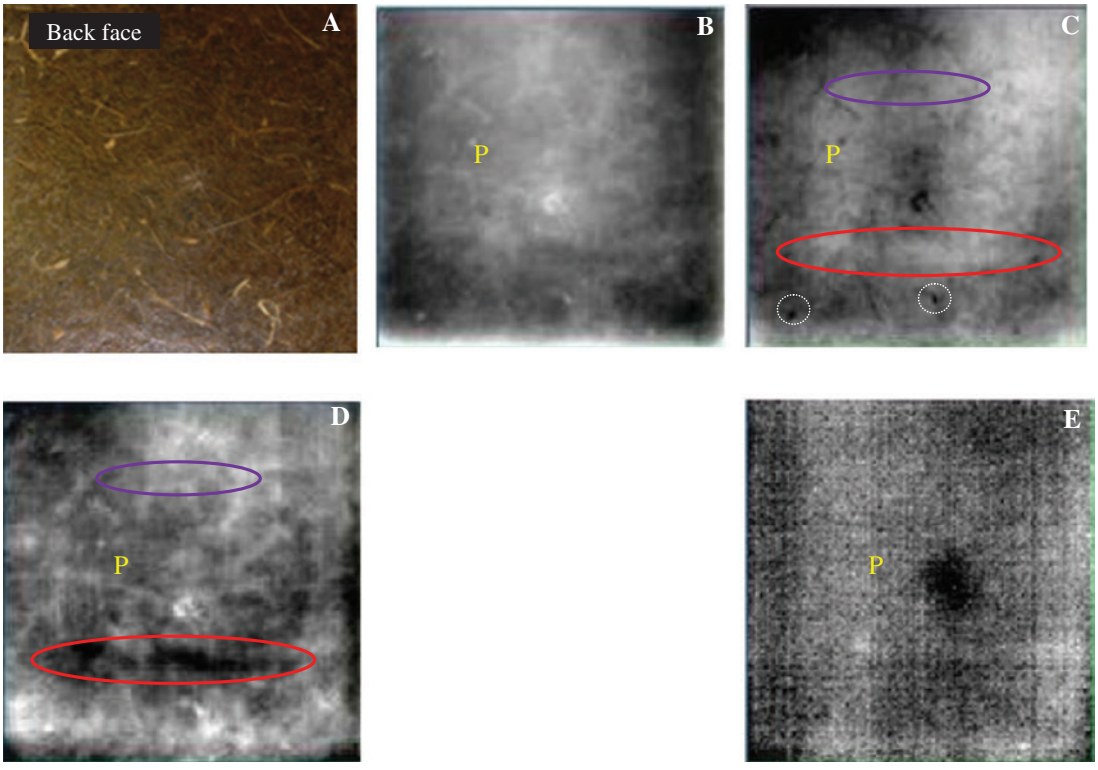

Figure 8 Selected PCT results of the sample (A) back of face, (B) EOF_3, (C) EOF_4, (D) EOF_6, (E) EOF_{14}.

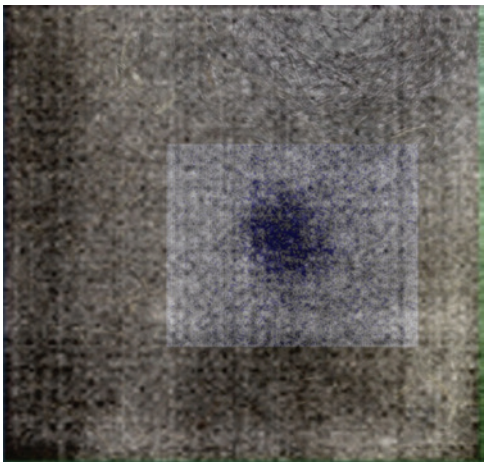

Figure 9 Fusion of images: 4B, 8A and E.

limit the spectrum from 0.7 to 0.9 μm, was used. The radiation source consisted of two halogen lamps (OSRAM SICCATHERM – 250 W IR) alternatively lit to perform reflectographic or transmittographic measurements. These lamps provide a wide spectrum radiation (including the NIR band) and were positioned facing each other with the laminate in the middle at the same distance from both lamps.

The right side of the sample exhibits a resin-starved area/lack of fibers marked by a dashed red rectangle (Figure 10). This area could be seen in Figure 10B and C, but not in reflection mode (Figure 10A), and its extension appears greater in transmission mode than by the image subtraction method (Figure 10B). This is due both to the thickness of the sample and to the technical characteristics previously explained.

Second, the area highlighted by a red oval in Figures 5, 8C and 8D is also confirmed by NIR technique. In this case, the image subtraction result shows the variability of the external fiber distribution inside this area: much denser in the right zone than on the opposite side. The same conclusion could be drawn comparing the T zone between Figure 10B and C.

The map of the zones where this method allows obtaining a clear indication of their real extension into the *x-y* Cartesian plan due to the lack of fibers in the *z* direction are highlighted by three dashed yellow arrows. In two cases, the results appear darker and, in another one, lighter depending on the amount of fibers distributed on the two external layers.

Taking into account the image subtraction result, the DT operator was applied, and the results are reported in Figure 11D, after a series of preprocessing steps (Figure 11A–C, E). The algorithm by Rosenfeld and Pfaltz [47], based on recursive morphology, is used in the present study [48].

The DT result enhances the zones of weakness of the sample shown in white (Figure 11D). The zone having a low concentration of fibers is linked to the white area, i.e., this result exalts the image's processing in Figure 10B. Instead, in Figure 11E, the watershed ridge line is reported; it shows the boundary of the resulting regions corresponding to the contours appearing in the first preprocessing image and on which ground the DT result is obtained. It is also possible to see as the P area (Figure 3A), i.e., where the indentation took place, is located in a zone with a high density of fibers, and this could justify the cross not affected by distortions obtained by the MatPIV 1.6.1 software (Figure 4A).

The DT result (Figure 11D) is very similar to that (Figure 12E) obtained applying the same morphological operator to the EOF_{10} (Figure 12A) as mentioned above. The steps linked to data processing, i.e., Figure 12B–D, F, are also included. A nonperfect correspondence among the matching pairs (Figure 11A–C, E) is apparent.

In particular, although the trend on the left zone of the sample appears very similar (Figures 11D and 12E), two additional light spots should be emphasized, respectively, surrounded by a dotted oval and marked by a

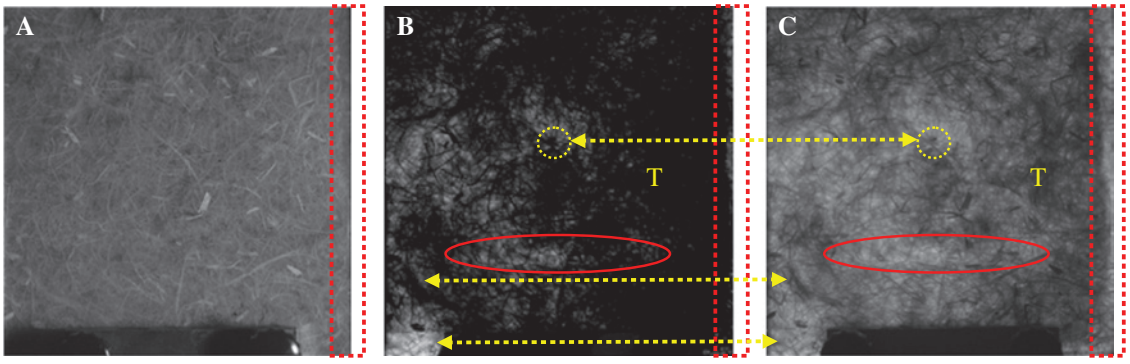

Figure 10 (A) NIR in reflection mode, (B) Image subtraction between (A) and (C), (C) NIR in transmission mode.

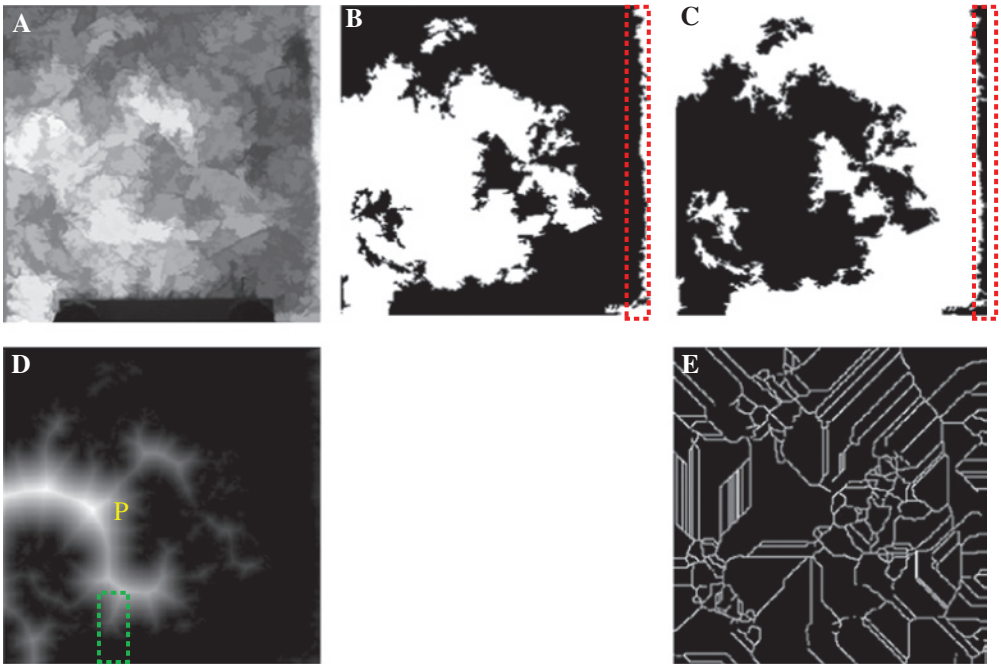

Figure 11 (A) Preprocessed image by morphological operator, (B) binary processing image, (C) complement of binary image, (D) distance transform, (E) image of watershed ridge line.

triangle. The dissimilarities could be explained considering that the approach proposed in Figure 11, already used in [90], explores the whole *z* axis through the plies, while the result proposed in Figure 12E is linked to a particular depth of the *z* axis. This is corroborated by the fact that part of the dotted green rectangle in Figure 11D is positioned on the stand and the remaining part on a defective area. This does not happen in Figure 12E, where the dotted green rectangle ends on a sound area.

However, the first light spot is confirmed working with the SWIR spectral band, and the visualization is enhanced in Figure 13, while the second light spot is linked to some of the data processing of the PT acquisition. Both deductions are discussed in the following.

The case of PCT-EOF_{10} technique merged with DT is improved with the aid of the marker-controlled watershed operator. The algorithmic definitions of the marker-controlled watershed transform have been given in various forms. Vincent and Soill developed a version called "simulated immersion", more suited to practical implementation: in this work, it fits very well to composite materials with real defects [70, 71]. Indeed, there is a one-to-one relation between the markers and the objects, that is, one marker should correspond to one object. This relation is very suitable to be applied in the case of PCT technique because there is a strict connection between the depth of a defect detected and the EOF explored [67].

Starting from the watershed ridge lines (Figure 12F) and knowing that an area close to the right side of the sample presents a lack of fibers, as discussed in Figure 10, it is possible to connect markers incorporating this parameter (Figures 12G, H) with a map summarizing the zones having a lack of fibers at a particular depth (Figure 12I). It is also noteworthy that the P area is not segmented, as this is rich in fibers, and the plies are compressed after the indentation test, i.e., the voids are filled. This is confirmed analyzing the speckles data by using the 2D-PIV software ver. 3.001-1.11 (Figure 4B).

The first light spot, surrounded by a dotted oval in Figure 12E, is enhanced by the top-hat transform, which is normally used for extracting small or narrow, bright or dark features in an image, whenever variations in the background impede achieving this by applying a threshold. The operator applied is visualized in 3D (Figure 13A) and 2D (Figure 13B) shapes.

In addition, comparing the result obtained applying the morphological operator (Figure 12B) and the result in Figure 13C, a much enhanced visualization of the nonwoven mat in hemp fiber is apparent (Table 2).

Many of the defects found by applying the optical and infrared NDT techniques described above are visible by the robust second-order blind identification (SOBI-RO) result (Figure 14). SOBI-RO algorithm combines robust whitening and time-delayed decorrelation [72]. Here, an ICALAB implementation was used [73].

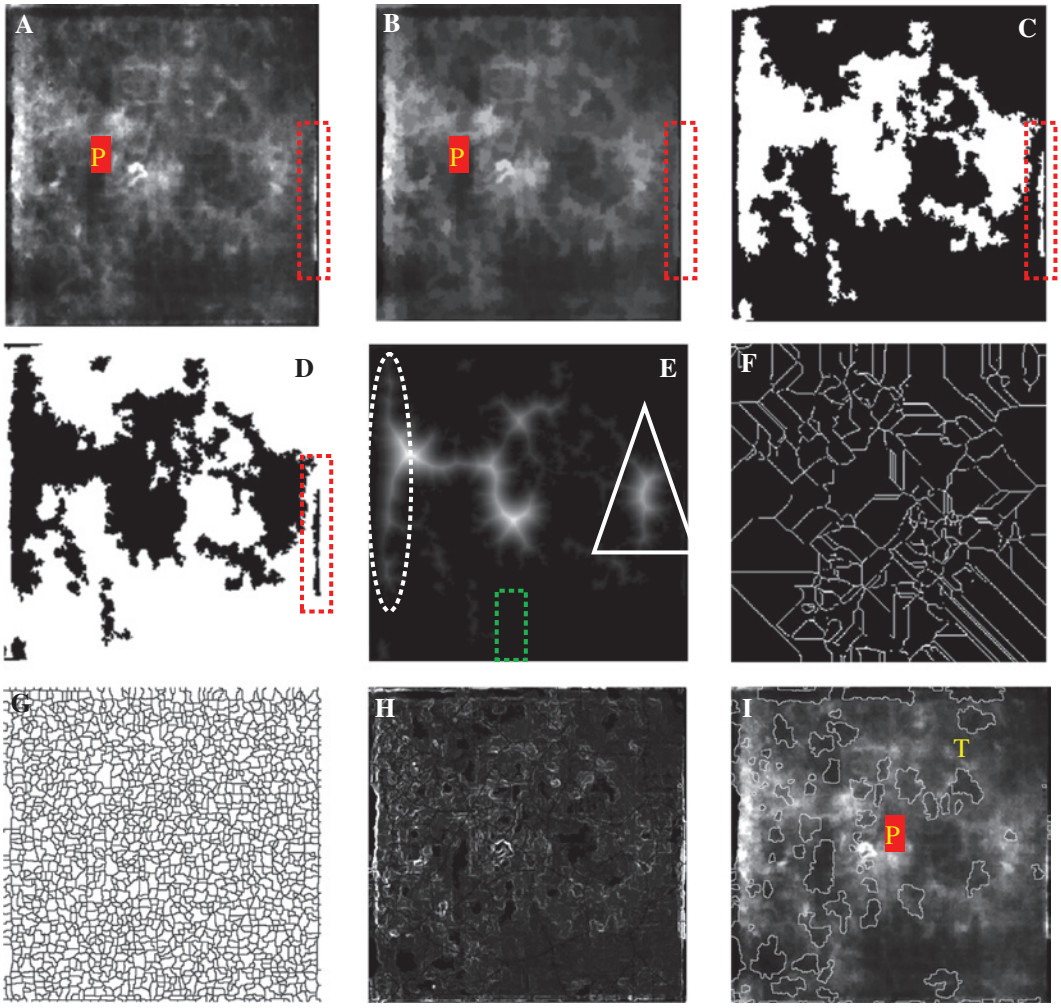

Figure 12 (A) EOF_{10}, (B) preprocessed image by morphological operator, (C) binary processing image, (D) complement of binary image, (E) distance transform, (F) image of watershed ridge line, (G) watershed – gradient, (H) watershed – gradient and marker controlled, (I) superimposed – watershed (GM) and original image.

This result comes from processing the SPT data to obtain the images shown in Figure 8. Figure 14 is very close to the result reported in Figure 8C (EOF_4), but the visualization of the upper left side, though too dark to be visualized, is legible in the SOBI-RO result. The shape and color of the indentation defect is the same in both figures; however, other dark spots appear in the SOBI-RO result, which are localized mostly in the lower part of the sample in addition to the two anomalies highlighted by dashed white circles in Figure 8C. The anomaly marked by a dashed yellow circle in Figure 14 is also present in Figure 10B with good contrast and, in Figure 10C, with lower contrast, while the lack of fibers in the area highlighted by a solid red oval and by the dashed red rectangle previously discussed (Figure 10B), are also confirmed.

The lack of fibers affecting the right side of the sample (see the dashed red rectangle in Figure 14) was not detected when applying the PCT algorithm (Figure 8), while it is very clear in the preprocessing results shown in Figure 11B and in C. The strut that is present during the NIR data acquisitions, and shown in Figure 10 (see the lower part of the sample), does not permit to detect the light spots related to a lack of fibers that are very clear in the SOBI-RO result (lower part), while partially visible in Figure 6B (dotted red circles).

To explore the potential of algorithms usually used after a PT acquisition [91] and corroborate the PCT results shown in Figure 8, PT data were processed applying PCT (Figures 15A–C) and PPT (Figure 15H) techniques. In this research, PT data was acquired with an IR camera working in the MWIR spectrum. To compare the result obtained in Figure 14 with other algorithms summarizing the information contained in a sequence into a single image, HOST (Figures 15D–G) and IR correlation techniques were also applied [53, 92].

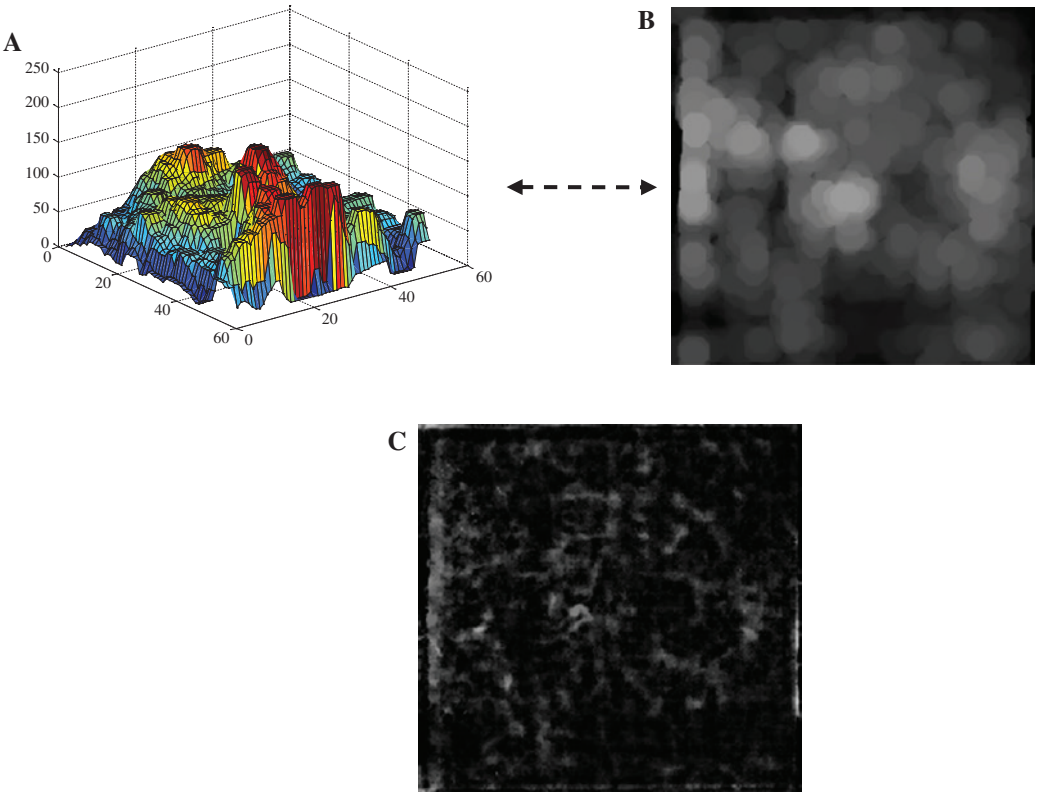

Figure 13 (A) Top-hat transform – 3D view, (B) top-hat transform – 2D view, (c) EOF_{10} after the top-hat treatment.

HOST extends second-order measures (such as the autocorrelation function and power spectrum) to higher orders to work on signals with non-Gaussian probability density function. An alternative method to higher-order statistical analysis is the use of a robust second-order blind identification (SOBI-RO) algorithm applied to SPT data (Figure 14).

Acquisition was carried out using an FPA infrared camera (Santa Barbara focal plane SBF125, Santa Barbara, CA, USA, 3 to 5 μm), on a 320 by 256-pixel array. The acquisition frequency used was set at 45 Hz. Two high-power flashes (Balcar FX 60), giving 6.4 kJ for a ~15-ms pulse, were used as heating sources in optical pulsed thermography. PT data was acquired in reflection mode as well as in the SPT experiment.

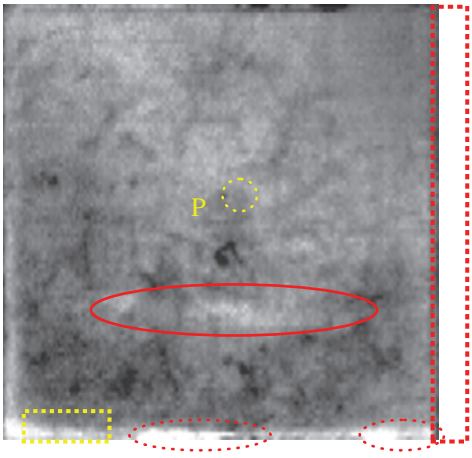

Figure 14 SOBI-RO result applying IR (SPT) data.

The good choice of the heating time is confirmed seeing the EOF_3 (Figure 15B), as after processing, the lack of fibers/resin-starved area along and close to three sides of the laminate was confirmed. This result was taken into consideration as the data input in the simulation by the COMSOL® program that was previously described (Figure 7).

In contrast, the other image processing methods (Figures 15A, C–H) were able to detect only one of the defects linked to the three sides, but not along the same side. The discontinuity surrounded by a red dotted oval in Figure 8C, D and in Figure 10B, C has been retrieved in four cases (Figure 15A, F, H, I), while a useful aid to characterize the existence of a larger amount of fibers on the right side of the sample, i.e., the T zone described in Figures 10B, C and 12I, is provided in Figure 15A, D, I, compared with the remaining zone, portioned by an irregular yellow line.

It is very surprising to note that the trend of the light spot surrounded by a triangle in Figure 12E is coincident

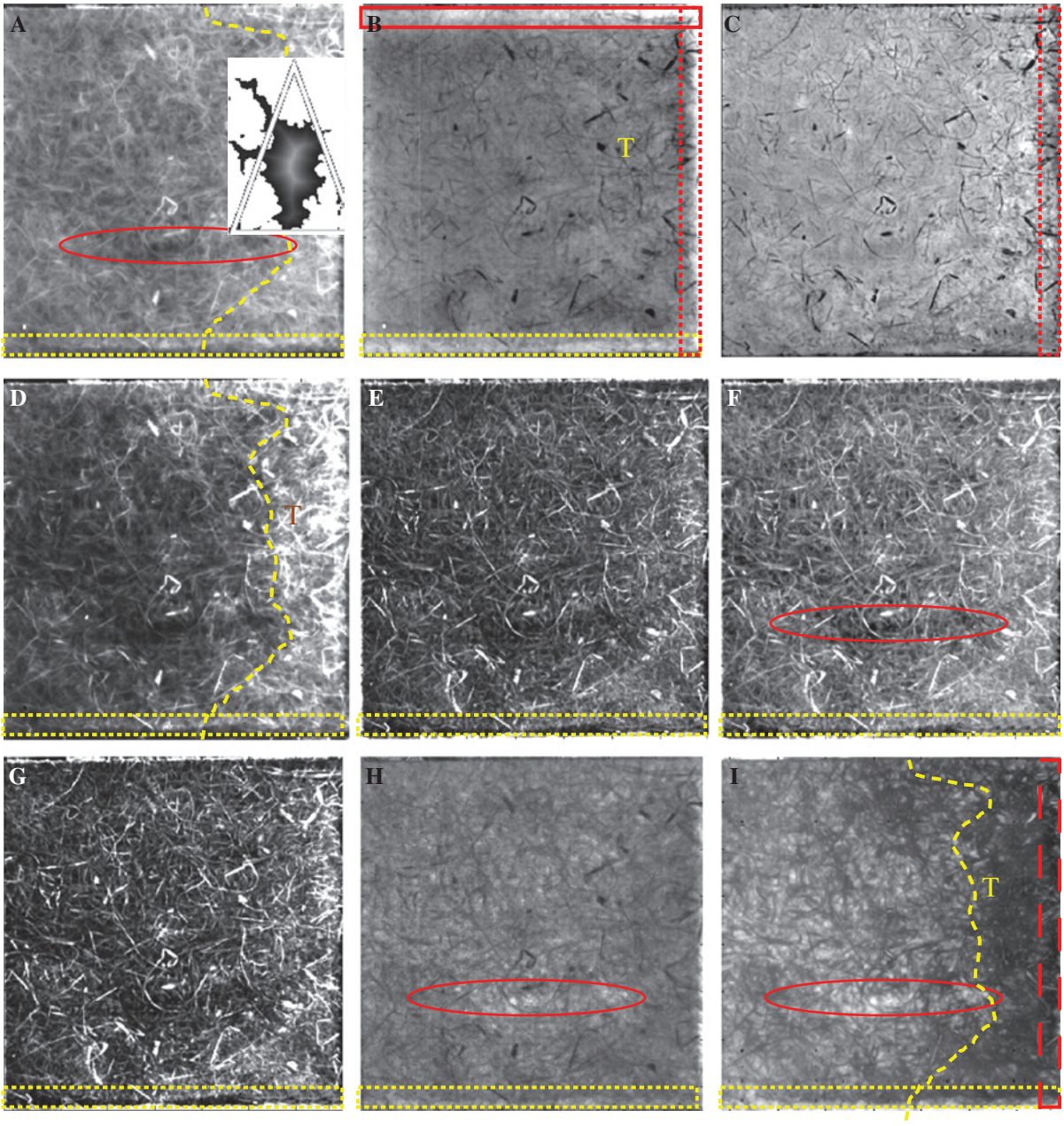

Figure 15 IRT results applying PT: (A) fusion of images: PCT-EOF$_2$ and DT result of Figure 12E, (B) PCT-EOF$_3$, (C) PCT-EOF$_4$, (D) HOST – second order, (E) Kurtogram, (F) skewness, (G) HOST – fifth order, (H) phasegram (f=0.88 mHz), (I) IR correlation.

to the trend of the irregular yellow line. This statement can be verified seeing Figure 15A, where the interesting area of Figure 12E was overlapped on Figure 15A in the right position. DT transform can act as a watershed operator: in the case under analysis, it divides the two zones like a border line, at least for the depth correlated to the EOF$_{10}$. The behavior shown by using second-order statistics thermography (SOST) technique (Figure 15D) is not due to a non-Gaussian signal because the same trend can be seen working with PCT (Figure 15A) and IR correlation (Figure 15I) algorithms: this is a key factor of the integrated approach proposed.

The IR correlation technique was chosen taking into account the hybrid nature of the sample material under testing. In particular, the correlation coefficient was used to indicate the strength and direction of the linear relationship between a given temperature evolution and the temperature evolution of all the pixels over the inspected sample, here computed using IR View [53].

In Figure 15I, it is possible to detect only three defects already detected in Figure 14. However, the quality of the detection of the inner layers is better than the SOBI-RO result (Figure 14) and is very close to the NIR result in

transmission mode shown in Figure 10C. This is surprising considering the different position of the lamps during the two NDT inspections, i.e., one in reflection and one in transmission mode.

After this inspection, the sample was analyzed utilizing a SWIR camera (Goodrich SU640SDWH-1.7 RT 640x512 pixels, InGaAs, UTC Aerospace Systems, Princeton, NJ, USA) and an incandescent bulb, which delivers wide spectrum IR radiation covering both nonthermal and thermal applications. The radiation source was combined with the utilization of narrow-band filters in order to limit radiation to the wavelength of interest. Figure 16 exhibits the SWIR results; the camera and the bulb were placed at the same distance during the acquisitions.

Comparing Figures 16A–E, it is obvious that the detection of the red or yellow-marked defects improves with increasing wavelength, from 940 to 1650 nm. In addition, the trend of the white zones shown in Figure 11D, detected when applying the DT operator to the NIR data, bears a good correspondence with the white areas shown in Figure 16E. A small region starting from the defect highlighted by a solid red oval to the defect marked by a dashed yellow rectangle must be integrated to the map shown in Figure 11D (in both figures, this area is highlighted by a dashed green rectangle). The stand hosting the sample during the NIR inspection did not allow its inspection in the lower side. In the case of the SWIR inspection, the detection of the P indented area was not identified with a good contrast as during the SPT data analysis by PCT (Figure 8) or applying the SOBI-RO operator (Figure 14). The perception of the different quantity of fibers (T area) between one side to another has a lesser impact (visually) compared to the NIR (Figure 10C) and/or PT data processing (Figure 15) results. Finally, it is very surprising to note the detection of the subsurface anomaly already revealed in Figures 10B, C and 14 (surrounded by a dotted yellow circle), which disappears only in Figure 16C, i.e., using a 1300-nm narrow-band filter. Considering the large amount of results obtained applying different NDT approaches on the same sample, a comparative table (Table 3) is introduced to summarize features detected by each processing technique with a general ranking. In particular, the symbols used are: (*), (**), (***), (^), which are combined with *defect or characteristic* clearly detected, detected, partially detected, and not detected, respectively. If a comparative approach is required, the two symbols reported on the same line have an identical yellow background.

4 Conclusions

In this study, a jute/hemp fiber hybrid laminate after an indentation test was investigated by optical, NIR/SWIR, and thermographic NDT inspections under laboratory

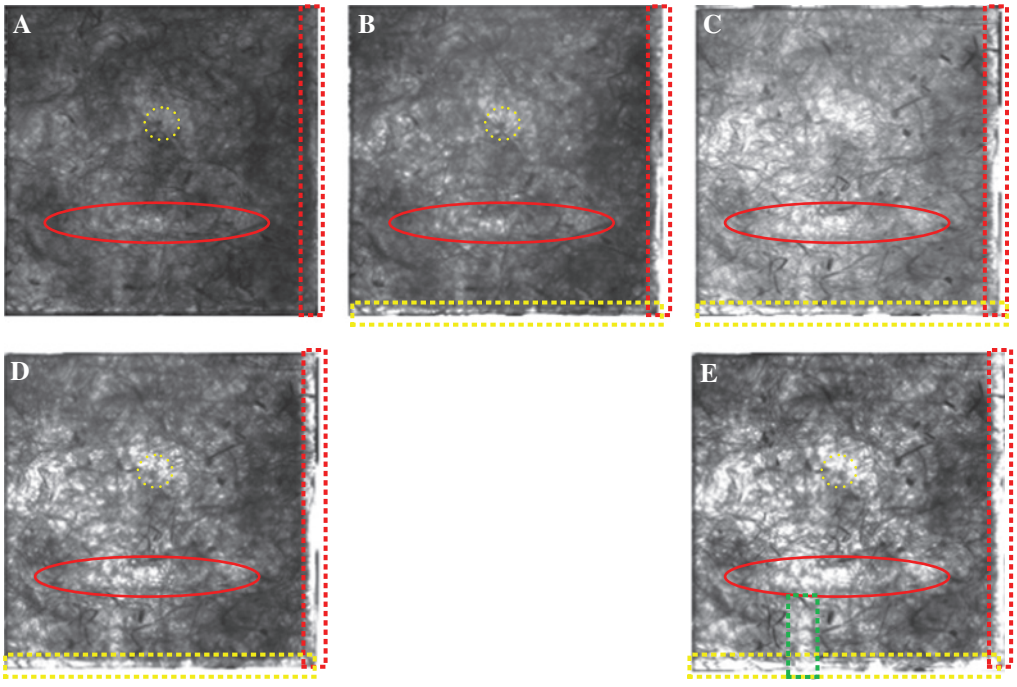

Figure 16 (A) SWIR 940 nm transmission mode (back face), (B) SWIR 1050 nm transmission mode (back face), (C) SWIR 1300 nm transmission mode (back face), (D) SWIR 1430 nm transmission mode (back face), (E) SWIR 1650 nm transmission mode (back face).

Table 3 Comparative table summarizing what was detected per each processing technique with a general ranking.

	MatPIV 1.6.1	2D-PIV	DE	Image subtraction	DT	Watershed T	Top-hat	NIRT	IR correlation	Raw thermogram	SOBI	PCT	PPT	HOST
Fiber distribution	***	‹	***	***	‹	‹	*	*	*	‹	***	***	**	**
Dent zone (comparative approach)	**	*	**	*	***	***	‹	***	‹	‹	***	*	‹	‹
Border areas with lack of fibers and/or resin-starved areas	‹	‹	‹	***	***	*	‹	*	**	***	**	*	***	***
Internal areas with lack of fibers and/or lack of adhesion between the fibers	***	‹	‹	**	*	*	‹	*	**	‹	**	***	**	***
Areas with higher concentration of fibers	‹	‹	‹	*	‹	***	‹	**	*	‹	‹	*	‹	*
Subsurface anomalies	‹	‹	‹	***	‹	‹	***	**	‹	‹	**	**	‹	‹
Confirmation of the Clark's theory (comparative approach)	*	‹	**	‹	‹	‹	‹	‹	‹	‹	‹	‹	‹	‹
Nature of the subsurface defect (comparative approach)	***	‹	‹	‹	‹	‹	‹	‹	‹	‹	‹	***	‹	‹
Boundary line	‹	‹	‹	***	**	‹	‹	***	**	‹	‹	**	‹	**

conditions and applying different operators (DT, top-hat transform, marker-controlled watershed, PCT, PPT, HOST, SOBI-RO, IR correlation, image subtractions).

Processing by PCT or SOBI-RO algorithm of the SPT data can provide results concerning the identification of the different subsurface defects due to the indentation test. On the other hand, to visualize the nonwoven hemp mat with higher image resolution and for detecting the zones where the sample has a lack of fibers, the use of NIR/SWIR is very useful, as well as the combined use of different techniques applied on PT data. EOF_{14} was also interesting to allow image fusion if applied together with DSP and the visible image, in order to confirm the shape of the subsurface damage provoked by the indentation test (P area). The use of advanced thermographic processing approaches, such as PCT, provided images seeing through the nonwoven mat of hemp, allowing identifying resin-starved areas or enhancing the difference between materials nature. In addition, PCT improved the quality and the visibility of the square pulse signal. The same consideration is true for PPT, PCT, HOST applied on a pulsed signal. On the other hand, HI can provide supplementary information about delaminations and/or cracks that occurred inside the samples.

DSP and the relative data processing by 2D-PIV software ver. 3.001-1.11 and MatPIV 1.6.1 software, was fundamental to confirm the different kinds of defects identified by other NDT methods. Thermal stress induced by a soldering iron was found to be optimal for both the nondestructive optical analysis methods.

Significant novelties of this work are a) Clark's theory has been confirmed for a composite material sample subjected to static indentation not reaching penetration, but resulting in internal damage; b) the combination of PCT, SOST, and IR correlation techniques to establish whether a laminate contains, or not, a different amount of natural fibers on a part of the inspected area; c) the use of a thermal simulation to provide the optimum heating time through a square pulse for the subsequent data processing; d) the use of DT to mark the boundary line between two zones having a different amount of fibers; e) the combination of PCT technique and marker-controlled watershed operator to reveal the zones with a lack of fibers/resin-starved at a particular depth; f) the use of top-hat transform to enhance the image contrast in zones of interest, e.g., the nonwoven hemp mat; g) the combination of PCT technique and DT as a useful alternative to the integrated approach among image subtractions and DT, already proposed in [90]. In particular, the DT applied to the NIR data acquired in transmission and reflection mode with image subtraction between both has offered a clear and complete map of the zones at low

indentation resistance due to a critical distribution of the jute fibers. Also, the use of the SOBI-RO algorithm applied on IR data appears very powerful for identification of small and subsurface defects; integration between the image subtraction algorithm and the IR correlation operator is also a good method to establish the zones of the sample with a higher concentration of fibers (T zone).

The combination of NDT techniques discussed in this work can be considered a promising tool for the assessment of composite materials made in natural fibers and to minimize false alarms, therefore, providing a great amount of information concerning the internal quality of these structures. Perspectives of this research include a) the experimental results obtained both in transmission and reflection mode in different spectral bandwidth will be reinforced by providing infrared (IR) and attenuated total reflection (ATR) spectroscopy characteristics; b) the use of probability of detection (POD) and receiver-operating characteristic (ROC) curves have been successfully applied to existing material manufacturing, but up to now, not for this type of materials [93]. The use of ROC curves to evaluate the potential of data fusion processes for this type of materials will be explored.

This combination of nondestructive testing methods allowed obtaining information about the presence of damage, resin-starved areas, and defects due to manufacturing techniques adopted and the inherent irregularities of the hierarchical structure of plant fibers. This appears promising especially whenever optimization techniques could be used to obtain the most suitable combination of NDT methods for the purpose, also by integrating the design of these experiments via, e.g., Taguchi matrices. This would assist the possible industrialization of this kind of controls on these sustainable composites, which are increasingly entering the market of structural applications.

References

[1] Caruso AP, De Rosa IM, Santulli C, Sarasini F. *E-Journal of Non Destructive Testing* 2010, 15, 1–7.
[2] Bledzki AK, Faruk O, Sperber VE. *Macromol. Mater. Eng.* 2006, 291, 449–457.
[3] Abrate S, *Impact on Composite Structures*, Cambridge University Press: USA, 1998.
[4] Ji B, Gao H. *J. Mech. Phis. Solids* 2004, 52, 1963–1990.
[5] McLaughlin EC. *J. Mater. Sci.* 1980, 15, 886–890.
[6] Eichhorn SJ, Baillie CA, Zafeiropoulos N, Mwaikambo LY, Ansell MP, Dufresne A, Entwistle KM, Herrera-Franco PJ, Escamilla GC, Groom L, Hughes M, Hill C, Rials TG and Wild PM. *J. Mater. Sci.* 2001, 36, 2107–2131.
[7] Joseph K, Tolědo Filho RD, James B, Thomas S, Hecker de Carvalho L. *Revista Brasileira de Engenharia Agrìcola e Ambiental* 1999, 3, 367–379.
[8] Santulli C. *J. Mater. Sci.* 2007, 42, 3699–3707.
[9] Sfarra S, Ibarra-Castanedo C, Santulli C, Paoletti A, Paoletti F, Sarasini F, Bendada A, Maldague X. *Compos Part B-ENG* 2013, 45, 601–608.
[10] Belouchrani A, Cichocki A. *Electron. Lett.* 2000, 36, 2050–2053.
[11] Belouchrani A, Abed-Merain K, Cardoso JF, Moulines E. *IEEE Trans. Signal Process.* 1997, 45(2), 434–444.
[12] Cichocki A, Shun-ichi A. *Adaptative Blind Signal and Image Processing Learning Algorithms and Applications*, John Wiley & Sons Ltd.: N.Y., 2003.
[13] Choi S, Cichocki A, Belouchrani A. *J. VLSI Signal Process.* 2002, 32, 93–104.
[14] Asseban A, Lallemand M, Saulnier JB, Fomin N, Lavinskaja E, Merzkirch W, Vitkin D. *Opt. Laser Technol.* 2000, 32, 583–592.
[15] Peters WH, Ranson WF. *Opt. Eng.* 1981, 21, 427–431.
[16] Chu TC, Ranson WF, Sutton MA. *Exp. Mech.* 1985, 25, 232–244.
[17] Sutton MA, Mingqi C, Peters WH, Chao YJ, McNeill SR. *Image Vis. Comput.* 1986, 4, 143–150.
[18] Sjodahl M. *Appl. Opt.* 1997, 36, 2875–2885.
[19] Pan B, Qian K, Xie H, Asundi A. *Meas. Sci. Technol.* 2009, 20, 1–17.
[20] Scarano F. *Meas. Sci. Technol.* 2002, 13, R1–19.
[21] Helm JD, McNeil SR, Sutton MA. *Opt. Eng.* 1996, 35, 1911–1920.
[22] Yamaguchi I. *Opt. Acta* 1981, 28, 1359–1376.
[23] Brillaud J, Lagattu F. *Appl. Opt.* 2002, 41, 6603–6613.
[24] Asundi A. *Opt. Lett.* 2000, 25, 218–220.
[25] Field JE, Walley SM, Proud WG, Goldrein HT, Siviour CR. *Int. J. Impact Eng.* 2004, 30, 725–775.
[26] Kirugulige MS, Tuppur HV, Denney TS. *Appl. Opt.* 2007, 46, 5083–5096.
[27] Siebert T, Becker T, Spiltthof K, Neumann I, Krupka R. *Opt. Eng.* 2007, 46, 051004.
[28] Duda, OR, Hart, PE. *Pattern Classification and Scene Analysis*, Wiley: N.Y., 1973.
[29] Périé JN, Calloch S, Cluzel C, Hild F. *Exp. Mech.* 2002, 42, 318–328.
[30] Sveen JK. *The MatPIV Home*, http://www.math.uio.no/~jks/matpiv, accessed on 26 September 2012.
[31] Astarita T. *Exp. Fluids* 2006, 38, 233–243.
[32] Astarita T. *Exp. Fluids* 2007, 43, 859–872.
[33] Tornari V. *J. Anal. Bioanal. Chem.* 2007, 387, 761–780.
[34] Heslehurst RB. *J. Adv. Mater.* 2009, 41, 5–12.
[35] Gryzagoridis J. *Int. J. Pres. Ves. Piping* 1992, 50, 317–335.
[36] Paoletti D, Schirripa Spagnolo G. *Meas. Sci. Technol.* 1990, 1, 1067–1071.
[37] Paoletti D, Schirripa Spagnolo G. *Progr. Opt.* 1996, 35 C, 197–255.
[38] Jaquot, P, Rastogi, PK. In *Fracture Mechanics in Concrete*, Wittmann FH, Ed., Elsevier Publishers BV: Amsterdam, 1983.
[39] Di Ilio A, Paoletti A, Paoletti D. *Comp. Sci. Tech.* 1997, 57, 365–369.
[40] Miller RA, Shah SP, Bjelkhagen HI. *Exp. Mech.* 1988, 28, 388–394.
[41] Mobasher B, Castro-Montero A, Shah SP. *Exp. Mech.* 1990, 30, 286–294.

[42] Sfarra S, Theodorakeas P, Ibarra-Castanedo C, Avdelidis NP, Paoletti A, Paoletti D, Hrissagis K, Bendada A, Koui M, Maldague X. *Insight* 2012, 54, 21–27.
[43] Sirohi RS, Radha Krishna HC. *Mechanical Measurements*, 3rd ed., New Age International (P) Ltd.: New Delhi, 1991.
[44] Vest CM. *Holographic Interferometry*, Wiley: N.Y., 1979.
[45] Pallav P, Diamond G, Hutchins D, Gan TH. *Insight* 2008, 50, 244–248.
[46] Daffara C, Fontana R. *Microsc. Microanal.* 2011, 17, 691–695.
[47] Rosenfeld A, Pfaltz J. *Pattern Recognit.* 1968, 1, 33–61.
[48] Fabbri R, Da Costa LF, Torelli JC, Bruno OM. *ACM Comput. Surv.* 2008, 40, 1–44.
[49] Ibarra-Castanedo C, Tarpani JR, Maldague XPV. *Eur. J. Phys.* 2013, 34, S91–109.
[50] Vavilov V. *Evaluating the Efficiency of Data Processing Algorithms in Transient Thermal NDT* (Proc. SPIE 5405-Thermosense XXVI, Orlando), 2004.
[51] Sun B, Ma Q, Zhao H. *Fitting-Correlation Analysis of Pulsed Thermographic Sequence Data* (Proc. of the IEEE, International conference on mechatronics and automation, Harbin), 2007.
[52] Vavilov V, Software ThermoFitPro, from Innovation Inc., http://www.innovation.tomsk.ru/ind_en.html, accessed on 23 January 2013.
[53] Klein M, Ibarra-Castanedo C, Maldague X, Bendada A. *A Straightforward Graphical User Interface for Basic and Advanced Signal Processing of Thermographic Infrared Sequences* (Proc. of the SPIE 6939-Thermosense XXX, Orlando), 2008.
[54] Maldague X, Marinetti S. *J. Appl. Phys.* 1996, 79, 2694–2698.
[55] Ishikawa M, Hatta H, Habuka Y, Fukui R, Utsumomiya S. *Infrared Phys. Technol.* 2013, 57, 42–49.
[56] Candoré, JC. *Détection et Caractérisation de Défauts par Thermographie Infrarouge* Stimulée: Application au Contrôle D'œuvres D'art, University of Reims: France, 2010.
[57] Grinzato E, Bison P, Marinetti S, Vavilov V. *Res. Nondestruct. Eval.* 1994, 5, 257–74.
[58] Bodnar JL, Candoré JC, Nicolas JL, Szatanik G, Detalle V, Vallet JM. *NDT&E Int.* 2012, 49, 40–6.
[59] Maldague, XPV. *Theory and Practice of Infrared Technology for Non-Destructive Testing*, John Wiley & Sons: N.Y., 1991.
[60] Balageas DL, Krapez JC, Cielo P. *J. Appl. Phys.* 1986, 59, 348–357.
[61] Ibarra-Castanedo C, Piau JM, Guilbert S, Avdelidis NP, Genest M, Bendada A, Maldague X. *Res. Nondestruct. Eval.* 2009, 20, 1–31.
[62] Sfarra S, Bendada A, Paoletti A, Paoletti D, Ambrosini D, Ibarra-Castanedo C, Maldague X, *Square Pulse Thermography (SPT) and Digital Speckle Photography (DSP): Non Destructive Techniques (NDT) Applied to the Defects Detection in Aerospace Materials* (Proc. of the 2nd International Symposium on NDT in Aerospace, Hamburg), 2010.
[63] Vavilov V, Kauppinen T, Grinzato E. *Res. Nondestruct. Eval.* 1997, 9, 181–200.
[64] Arndt RW. *Infrared Phys. Technol.* 2010, 53, 246–253.
[65] Pearson K. *Philos. Mag.* 1901, 2, 559–572.
[66] Hotelling H. *J. Educ. Psych.* 1933, 24, 417–441.
[67] Rajic N. *Compos. Struct.* 2002, 58, 521-528.
[68] Marinetti S, Grinzato E, Bison PG, Bozzi E, Chimenti M, Pieri G, Salvetti O. *Infrared Phys. Technol.* 2004, 46, 85–91.
[69] Bai X, Zhou F, Bindang X. *Opt. Laser Technol.* 2012, 44, 328–336.
[70] Soille P. *Morphological Image Analysis: Principles and Applications*, II Ed., Springer-Verlag: Germany, 2004.
[71] Vincent L, Soille P. *IEEE Trans. Pattern Anal. Mach. Intell.* 1991, 13, 583–98.
[72] Choi S, Cichocki A, Park H-m, Lee S-Y. *Neural Inf. Process. Lett. Rev.* 2005, 6, 1–57.
[73] Cichocki A, Amari S, Siwek K, Tanaka T, Phan AH, Zdunek R, Cruces S, Georgiev P, Washizawa Y, Leonowicz Z, Bakardjian H, Rutkowski T, Choi S, Belouchrani A, Barros A, Thawonmas R, Hoya T, Hashimoto W, Terazono Y. *ICALAB Toolboxes*, http://www.bsp.brain.riken.jp/ICALAB, accessed on 08 April 2012.
[74] Santulli C, Cantwell WJ. *J. Mater. Sci. Lett.* 2001, 20, 477–479.
[75] Santulli C, Caruso AP. *Malaysian Polym. J.* 2009, 4, 19–29.
[76] Clark G. *Composites* 1989, 20, 209–214.
[77] Peters, RH. *Tensile Chemistry. Vol. I: The Chemistry of Fibers*, Elsevier: N.Y., 1963.
[78] Winkler F. *Acta Polymerica* 1981, 32, 666.
[79] Sreepathi LK, Ahmed KS, Vijayarangan S. *Measurement of Thermal Conductivity of Jute Fiber Reinforced Polyester Composites* (Proc. of the National Conference on Advanced Mechanical Engineering, Karnataka), 2010.
[80] Wieland, H, Murphy DPL, Behring H, Jäger C, Hinrichs P, Bockisch F-J. *Landtechnik* 2000, 55, 22–23.
[81] Kauriinvaha E, Viljanen M, Pasila A, Kymäläinen HR, Pehkonen A. *Bio-Fiber From Field to Thermal Insulation of Building* (Helsinki University of Technology-Laboratory of Structural Engineering and Building Physics, Espoo) 2001.
[82] Suardana NPG, Piao Y, Lim J-K. *Mat. Phys. Mech.* 2011, 11, 1–8.
[83] Zach J, Hroudova J. *Utilization of Technical Hemp for Thermal Insulating Materials Production* (Proc. 2nd Int. conf. on sustainable construction materials and technologies, Ancona), 2010.
[84] Michalak M, Więcek B, Kruciñska I. *Modelling and Thermography Measurements of Thermal Properties of Nonwovens* (Proc. of the 5th QIRT, Dubrovnik), 2002.
[85] Mutnuri B. *Thermal Conductivity Characterization of Composite Materials, Thesis for the Master of Science in Mechanical Engineering* (Department of Mechanical Engineering, Morgantown), 2006.
[86] Akil H Md, De Rosa IM, Santulli C, Sarasini F. *Mat. Sci. Eng. A-Struct.* 2010, 527, 2942–2950.
[87] Springer GS, Tsai SW. *J. Compos. Mater.* 1967, 1, 166–173.
[88] Jopek H, Strek T. In *Convection and Conduction Heat Transfer*, Ahsan A, Ed., InTech Publisher Croatia: Rijeka, 2011.
[89] Sfarra S, Ibarra-Castanedo C, Lambiase F, Paoletti D, Di Ilio A, Maldague X. *Meas. Sci. Technol.*, 2012, 23, 115601 (14 pp).
[90] Sfarra S, Ibarra-Castanedo C, Santulli C, Sarasini F, Ambrosini D, Paoletti D, Maldague X. *Strain* 2013, 49, 175–189.
[91] Ibarra-Castanedo C, Avdelidis NP, Grenier M, Maldague X, Bendada A. *Active Thermography Signal Processing Techniques for Defect Detection and Characterization on Composite Materials* (Proc. of the SPIE 7661-Thermosense XXXII, Orlando), 2010.
[92] Madruga FJ, Ibarra-Castanedo C, Conde OM, Lopez-Higuera JM, Maldague X. *NDT&E Int.* 2010, 49, 661–666.
[93] Duan Y, Servais P, Genest M, Ibarra-Castanedo C, Maldague X. *J. Mech. Sci. Technol.* 2012, 26, 1985–1991.